NJC

ROYAL SOCIETY OF CHEMISTRY

PAPER

View Article Online
View Journal | View Issue

Cite this: *New J. Chem.*, 2020, **44**, 13249

Rhodium nanoparticles impregnated on TiO_2: strong morphological effects on hydrogen production†

Brunno L. Albuquerque, *[a] Gustavo Chacón,[a] Michael Nazarkovsky[b] and Jairton Dupont[a]

Received 13th May 2020,
Accepted 28th June 2020

DOI: 10.1039/d0nj02419h

rsc.li/njc

The effect of the shape of rhodium nanoparticles impregnated on TiO_2 on photocatalytic hydrogen generation using methanol as a sacrificial reagent has been investigated by using a simple home-made UV-LED light strip reactor to activate the catalyst surface. For rhodium nanocubes, the normalised rate of H_2 production was 22.4 mmol h^{-1} m^{-2} at 365 nm and 7.5 mmol h^{-1} m^{-2} at 400 nm. The normalised activity/surface area of the studied Rh nanoparticles showed a trend that led to establishing a relationship between the exposed [100] facets and photocatalytic activity. The Rh shape-dependent H_2 production follows a trend of cubic > spherical > octahedral, which is associated with a higher surface energy of the Rh nanoparticles.

1. Introduction

The process of photocatalytic hydrogen production using TiO_2 as a catalyst and Pt as a co-catalyst under UV irradiation was reported almost half a century ago.[1,2] Since then, huge efforts have been dedicated to the development of new materials capable of being activated with the visible region of the solar spectrum for a diverse set of applications such as hydrogen production,[3–5] CO_2 reduction,[6–8] and decomposition of organic dyes,[9–11] amongst others. The emission of the solar spectrum in the UV region accounts for only about 3–4% of all the light that reaches the Earth's surface.[12] However, the advent of newer technologies of light-emitting diodes (LEDs) allows for the use of common photovoltaic cells and, hence, UV absorbing semiconductors can be used without modification to harvest photons in the visible region indirectly.[13,14]

Although there have been several investigations regarding the composition of the co-catalyst in H_2 production,[15–17] only a few specific studies about the crystal morphology and nanoparticle shape *vs.* activity have been reported thus far.[18–23] With the recent development of shape-controlled synthesis of nanocrystals,[24–27] a new field for catalysis has been opened for a plethora of specific transformations.[28,29] The effect of octahedral and cubic Pd nanoparticles impregnated on TiO_2 has been investigated on water photolysis using various alcohols as sacrificial agents and it was shown that exposed Pd[111] facets increased the heterojunction between the metal and semiconductor, thus enhancing hydrogen production.[30] However, an overall higher trend for H_2 production was demonstrated to be directly related to the [100] facets of cubic nanoparticles.[31–33] For Rh nanoparticles deposited over graphitic carbon (g-C_3N_4), there is no size dependence for hydrogen production in aqueous methanol. It was hypothesized that metallic Rh was essential for the removal of photogenerated electrons at the surface.[34] Additionally, studies on the effect of the size of Rh nanoparticles on GaN:ZnO in a sulfuric acid solution for photocatalytic water splitting indicated that the activity of Rh@Cr_2O_3 core–shell nanoparticles (NPs) is dependent upon the size of the Rh core.[35] It is known that upon variation of the size of the nanocrystal, the ratio of atoms in the edges, corners, faces and vertices is not constant; hence, the normalisation of the surface atoms by using metallic nanoparticles should be corrected.[36]

In this study, we report the development of Rh NPs with different shapes as co-catalysts in the photocatalytic reforming of methanol for the production of hydrogen in aqueous media. Three different Rh NP shapes were studied (cuboctahedra RhNP, cubic RhNC and octahedral RhOh) to evaluate the surface composition activity by using the magic number approach (Fig. 1).[36] The catalysts were characterized by standard techniques such as electron microscopy and the textural and electronic properties were studied. Also, the LED reactor lamp which permitted this study was developed.

[a] *LAMOCA – Laboratory of Molecular Catalysis, Institute of Chemistry – Universidade Federal do Rio Grande do Sul., Av. Bento Gonçalves, 9500 Porto Alegre, 91501-970 RS, Brazil. E-mail: brunno.albuquerque@ufrgs.br*

[b] *Pontifícia Universidade Católica de Rio de Janeiro, Rua Marquês de São Vicente, 225, Rio de Janeiro, 22451-900 RJ, Brazil*

† Electronic supplementary information (ESI) available. See DOI: 10.1039/d0nj02419h

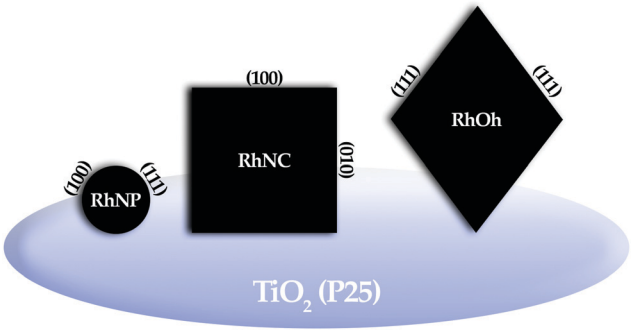

Fig. 1 Illustration of the Rh nanoparticle shapes used in this work showing the lattice planes of the exposed facets.[37]

2. Experimental

2.1. Materials and methods

Rhodium chloride ($RhCl_3$) was purchased from Stream Chemicals, 2-bromoethanol was purchased from Oakwood Chemical China, and TiO_2 aeroxide (P25) was obtained from Evonik Industries. 1-Methyl imidazole was obtained from Spectrum Chemical and distilled under reduced pressure prior to use. Rhodium acetate dimer ($Rh_2(OAc)_4$) and the other reagents were purchased from Sigma-Aldrich (Merck) and used without further purification. Methanol was HPLC grade and deionized water (18.2 MΩ cm) was used throughout this study.

2.2. Reactor lamp design and reaction Schlenk vessel

Two reactors were built by using 300-LED strips with emission at 365 ± 5 nm and 400 ± 10 nm. These strips were glued to the inner side of a cylinder (∅ = 15 cm, 15 cm height) where the top part was fitted with three small fans (60 mm) for forced ventilation (see Fig. S1a and b for illustration, ESI†). The power output of each strip is 20 W and 24 W at 365 nm and 400 nm, respectively. Both of the lamps were powered by the same 12 V, 20 amp power supply. The reaction vessel consisted of a Schlenk tube adapted with a GC septum for gas sampling as shown in Fig. S1c (ESI†).

2.2.1. Determination of the UV-LED photon flux. The photon flux of the UV-LED reactor assembly was measured using ferrioxalate actinometry adapted from the literature.[38] Three stock solutions were prepared using distilled water. Stock solution **A** was prepared by dissolution of 0.967 g of $Fe(NO_3)_3 \cdot 9H_2O$ (0.4 mol L^{-1}) in 10 mL of water. Oxalate stock solution **B** was prepared by dissolution of 2.0 g of $K_2C_2O_4$ (1.2 mol L^{-1}) in 10 mL of water. Stock solution **C** was prepared by dissolution of 10 mg of 1,10-phenantroline (5.5 mmol L^{-1}) and 2.245 g sodium bicarbonate (1.65 mol L^{-1}) in 10 mL of H_2O. Stock solutions A and C were protected from light.

The reaction solution was prepared by a mixture of 1.0 mL of solution **A** and **B**, diluted to 20 mL in darkness. Then, 10 mL of the reaction solution was transferred to the Schlenk tube used in the photocatalytic experiments equipped with a magnetic stirring bar and then irradiated for 5 min. After this time, 0.5 mL was taken from the reaction solution, mixed with 0.5 mL of stock solution **C** and diluted to 5 mL with H_2O. The spectrum was measured before and after the irradiation and the absorption at 510 nm used for quantification of the Fe^{2+} formed. The photon flux was calculated by the formula:

$$n_{Fe^{2+}} = \frac{V_1 V_3 \Delta A}{V_2 l \varepsilon} \quad (1)$$

where V_1 is the volume of the irradiated solution (10 mL), V_2 is the volume taken from the reaction solution (0.5 mL) and V_3 is the volume measured in the UV-vis (5 mL). ΔA is the variation of maximum absorbance measured at 510 nm before and after irradiation, l is the optical path length of the cuvette (l = 1.0 cm) and ε is the molar extinction coefficient for $[Fe(phen)]^{2+}$ (11 100 L^{-1} mol^{-1} cm^{-1} at 510 nm). The number of incident photons is calculated by the formula:

$$\frac{n_{photons}}{min} = \frac{n_{Fe^{2+}}}{\Phi_\lambda t F} \quad (2)$$

where Φ is the quantum yield of Fe^{2+} production (Φ_{365} = 1.270 and Φ_{400} = 1.188),[39] t is the irradiation time (5 min) and F is the mean fraction of absorbed light (F = 1).

2.3. Synthetic procedures

2.3.1. Synthesis of BMIm·OAc. Previously, BMIm·Cl was prepared by reacting butyl chloride and 1-methylimidazole at 75–80 °C for 48 hours. After recrystallization in an acetone/methanol mixture, BMIm·Cl was obtained as white crystals (yield: 80%). ^{1}H NMR (400 MHz, D_2O) δ ppm 0.89 (*t*, J = 7.4 Hz, 3H); 1.22–1.35 (m, 2H); 1.82 (qp, J = 7.4 Hz, 2H); 3.86 (s, 3H); 4.17 (t, J = 7.2 Hz, 2H); 7.40 (d, J = 2.0 Hz, 1H); 7.45 (d, J = 2.0, 1H). In a second step, the corresponding BMIm·OAc was obtained by anion exchange using Amberlyst X resin saturated with OH^- ions. After the anion exchange, glacial acetic acid was added and the produced water removed under a vacuum to obtain BMIm·OAc as a pale-yellow oil. Yield: 80%. NMR analysis. ^{1}H NMR (400 MHz, $CDCl_3$) δ ppm 0.97 (t, J = 7.4 Hz, 3H); 1.31–1.41 (m, 2H); 1.83–1.89 (m, 2H); 1.97 (s, 3H); 4.05 (s, 3H); 4.23 (t, J = 7.4 Hz, 2H); 7.24 (s, 1H); 7.30 (s, 1H); 11.08 (s, 1H). The residual water content was determined by Karl–Fischer titration (3%).

2.3.2. Synthesis of HEMIm·Br. In a typical procedure, in a round bottomed flask equipped with a magnetic stirrer 10 mL of 1-methylimidazole (0.125 mol) and 10 mL of 2-bromoethanol (0.141 mol) were mixed at room temperature. After 48 h the reaction flask was cooled until precipitation of HEMIm·Br was induced. Then, the resulting solid was washed with diethyl ether and dried under a vacuum. Yield: 83%, NMR analysis. ^{1}H NMR (400 MHz, D_2O) δ ppm; 3.80 (s, 1H); 3.84 (m, 2H); 4.64 (s, 2H); 7.35 (t, J = 2.0 Hz, 1H); 7.40 (t, J = 2.0, 1H).

2.3.3. Preparation of spherical rhodium-impregnated TiO_2 (RhNP). The RhNP were prepared by chemical reduction with $NaBH_4$. Typically, 8.0 mg of $Rh_2(OAc)_4$ (0.036 mmol in Rh) was dissolved in a solution containing 75.0 mg of BMIm·OAc (0.38 mmol) in 40 mL of deionized water. After 30 minutes under vigorous stirring, 10 mL of a freshly prepared ice-cold $NaBH_4$ solution in deionized water (7.0 mg of $NaBH_4$, 0.185 mmol) was added to the solution. After a few minutes,

the initial blue colour turns to dark brown, characterizing the formation of Rh@BMIm·OAc.

The impregnation of Rh nanoparticles on TiO_2 procedure was adapted from the literature.[40] In a typical experiment, 1000 mg of TiO_2 (Evonik, P25) freshly macerated in an Agatha mortar was added to 50 mL of the Rh@BMIm·OAc colloidal solution under vigorous stirring during 48 hours. After this time, RhNP were isolated by centrifugation, washed with deionized water, and dried under a vacuum at 60 °C for 12 hours (isolated yield: 917 mg).

2.3.4. Preparation of cubic rhodium-impregnated TiO_2 (RhNC). The rhodium nanocubes were synthesized as follows: 42.0 mg of $RhCl_3$ (0.2 mmol), 444.5 mg of PVP (55 Da, 4.0 mmol in monomer units) and 207.1 mg of HEMIm·Br (1.0 mmol) were placed in a Schlenk tube and dissolved in ethylene glycol. This mixture was heated to 80 °C for 20 minutes under vigorous stirring. After this time, the resulting solution was placed in a silicone bath at 185 °C and the reaction conducted for 1.5 h. After this, acetone was added and the solution centrifuged to obtain a precipitate, which was re-dissolved with a few drops of ethanol and acetone in order to remove remaining PVP. RhNC were recovered by centrifugation and dried under a vacuum (isolated yield: 20.0 mg).

For impregnation of rhodium nanocubes on TiO_2, 5.0 mg of the previously isolated powder was dissolved in 25 mL of water and added dropwise to a solution of 1000 mg TiO_2 in 25 mL of water. After addition, the resulting solution was stirred for 48 h at room temperature, and RhNC isolated by centrifugation. The RhNC were washed with deionized water, and dried under a vacuum at 60 °C for 12 hours (isolated yield: 800 mg).

2.3.5. Preparation of octahedral rhodium-impregnated TiO_2 (RhOh). In a typical synthesis, PVP (55 Da, 33.3 mg, 0.29 mmol in monomer units), ascorbic acid (480 mg, 2.72 mmol) and citric acid (60 mg, 0.31 mmol) were dissolved in 9.0 mL of ethylene glycol under magnetic stirring at 145 °C. In another flask, $RhCl_3$ (6.2 mg, 0.03 mmol) was totally dissolved in 2.0 mL of ethylene glycol and then added to the PVP, ascorbic acid and citric acid solution mixture. The reaction was carried out at 145 °C for 2 hours. After cooling to room temperature, the solution was centrifuged and washed with ethanol to remove the excess PVP. Finally, the octahedral rhodium nanoparticles were isolated by centrifugation at 12 000 rpm (yield: 5 mg). The same RhNC impregnation procedure on TiO_2 was used for RhOh (isolated yield: 740 mg).

2.4. Rh nanoparticle characterization

The TEM samples were prepared by drop-casting the colloidal nanoparticles and the supported catalyst onto Cu grids (holey carbon – EMS), 300 mesh. The TEM images were acquired using a JEOL JEM 1011 electron microscope operating at 100 kV using at least 400k magnification. The HRTEM and HAADF-STEM images were acquired using a JEOL JEM 2100F electron microscope operated at 200 kV equipped with an Oxford Instruments X-Max^N 80 LTE EDS detector, which was used for elemental mapping with STEM imaging. For elemental mapping, the sample holder was tilted 17.0° towards the detector for a better signal-to-noise ratio and the EDS maps were acquired in the range of 0 to 40 keV. The Kα_1 emission line was chosen for the composition of the colour map of the elements, Rh at 20.217 keV and Ti at 4.508 keV. The as-prepared colloidal samples were isolated by centrifugation, dried under a vacuum and analysed by X-ray photoelectron spectroscopy (XPS) using Al-Kα radiation and a Scientia Omicron hemispherical analyser. Adventitious C 1s (284.8 eV) was used as a reference. Textural characterization was performed using low-temperature N_2 adsorption–desorption isotherms (Tristar Kr 3020, Micromeritics). Prior to the measurements, the samples were degassed at 120 °C under a vacuum for 12 h. The specific surface area, S_{BET}, was determined by the BET (Brunauer, Emmett and Teller) multipoint technique.[41] The total pore volume, V_p, was calculated at the maximal adsorption point (p/p_0 = 0.98–0.99). The pore size distribution by volume (PSDV) was computed through self-consistent regularization under non-negative conditions of the pore size distribution function, $f(R_p) > 0$, and with a regularization parameter α = 0.01. The method allows us to estimate the contributions of different pore types based on their size: micro- (V_{micro} at $R_p < 1$ nm), meso- (V_{meso} at 1 nm $< R_p <$ 25 nm) and macropores (V_{macro}, $R_p > 25$ nm). The mathematical approach are discussed in detail in ref. 42–45. The fractality was determined from the Frenkel–Halsey–Hill (FHH) method involving the isotherm's adsorption branch within $p/p_0 < 0.8$. The fractal dimension D_S was calculated from the plot corresponding to the equation $\ln(V/V_0) = (D_S - 3)\cdot\ln[\ln(p_0/p)]$ + const, where V and V_0 are the volume of adsorbed N_2 and the saturation volume of adsorbed N_2, respectively, and p and p_0 are the equilibrium and saturation pressure of adsorbed nitrogen, respectively.

The electronic properties of Rh impregnated on TiO_2 were measured by UV-vis diffuse reflectance spectroscopy using a Shimadzu UV2100 equipped with an integrating sphere accessory. Powder samples were packed into the sample holder and measured against $BaSO_4$ as a standard.

2.5. Photocatalytic H_2 production experiments

In a reactor vessel, 10 mg of the corresponding catalyst was dissolved in 9 mL of deionized water and 1 mL of methanol. The mixture was sonicated for 30 s at 1000 W in order to disperse the catalyst and the solution was deaerated by bubbling argon with a stainless-steel needle during 20 minutes. After this time, the reactor was placed in the UV-LED reactor and periodic samples of the headspace analysed (H_2, CO, CH_4 and CO_2 content) with the aid of a gastight syringe (100 μL) in a GC equipped with a TCD detector. The production of CO and CH_4 is negligible, but the overall production of CO_2 is about 1/3 of the production of H_2, as a sub-product of methanol oxidation.

The relative photonic efficiency (ζ_r)[46] was estimated by using formula (3) below, which correlates the amount of H_2 produced, considering a $2e^-$ reaction, with the photon flux measured by ferrioxalate actinometry.

$$\zeta_r(\%) = \frac{2n\ \mathrm{H_2\ produced}\ (\mu\mathrm{mol\ min^{-1}})}{n\ \mathrm{photons}\ (\mathrm{min^{-1}})} \times 100 \qquad (3)$$

3. Results and discussion

3.1. UV-LED lamp reactor and actinometry

In this work a home-made UV-LED reactor was used as a light source which is low cost and has low energy consumption in comparison to other types of light sources and high intensity monochromatic emission.[47,48] Ferrioxalate actinometry was used to probe the photon flux of the UV-LED reactor and in Fig. 2 is shown the UV/vis spectra after/before 5 minutes of irradiation at both wavelengths studied here. Using an absorbance value of 510 nm the photon flux of each UV-LED strip was estimated, as shown in Table 1.

3.2. Rh–TiO_2 characterization

The average size distribution and the morphology of the Rh nanoparticles were probed by conventional TEM (Fig. 3). As expected, the chemical reduction of Rh by $NaBH_4$ afforded very small spherical nanoparticles with a narrow size distribution. The cubic and octahedral nanoparticles were prepared by polyol solvolysis at high temperature using Br^- ions and citrate as shape inducers. The mean size and distribution of the nanoparticles are summarized in Table 2. RhNC were measured diagonally, while RhOh were measured by the longest length of the nanoparticles.

As the statistical analysis of the Rh nanoparticle size distribution has shown (Fig. S2, ESI†), all three samples are characterized by a strict tendency in the average diameter growth together with the standard deviation in the RhNP–RhNC–RhOh series. This, in turn, speaks to a less dispersed character of the spherical nanoparticles – the standard deviations (SDs) for RhNC and RhOh are as high as *ca.* 2 and 4 in comparison to the SD for RhNP. The enlargement of the interquartile range (0.4875, 0.9563, and 2.47 for RhNP, RhNC and RhOh, respectively) and normal character for non-spherical particles may favour a view that the polyol affected synthesis procedures for RhNC and RhOh occur stochastically, *i.e.*, in both cases, the formation of larger nanoparticles required more time to achieve the equilibrium. The reduction in the presence of $NaBH_4$ for RhNP could be controlled kinetically, resulting in enhanced selectivity with a set nanoparticle size. Taking a closer look at the distribution profiles, RhNC and RhOh demonstrate normality validated by the D'Agostino–Pearson test, revealing $p_{D-P} > 0.05$ (0.275 and 0.068, respectively). Contrastingly, RhNP have not passed the normality test at $p_{D-P} \ll 0.05$ (Fig. S2, ESI†).

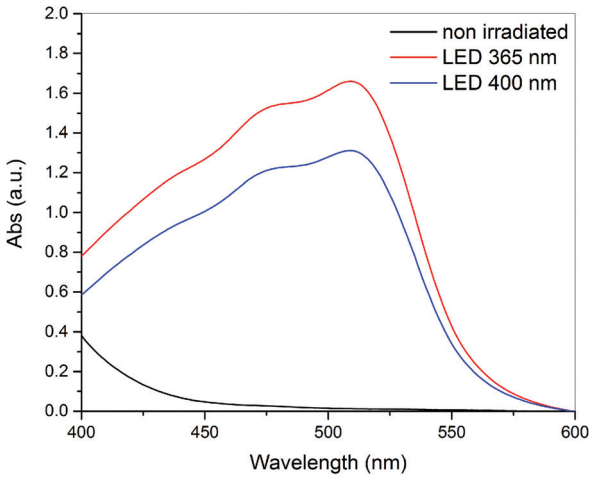

Fig. 2 UV-vis spectra of ferrioxalate actinometry, before (black line) and after irradiation (red line) using a 365 nm UV-LED and (blue line) using a 400 nm UV-LED.

Table 1 Measured photon flux of each UV-LED assembly

Lamp reactor	ΔA	Photon flux (photons $min^{-1} \times 10^{-6}$)
365 nm	1.56	2.22
400 nm	1.25	2.06

After impregnation on TiO_2, the catalysts were characterized by HRTEM as shown in Fig. 3. For RhNC and RhOh it was possible to measure the lattice spacing of the Rh and TiO_2, Fig. 3e and f, and the measured distances by FFT are in accordance with the fcc structure of Rh. The lattice planes of RhNC and RhOh show contributions of the (200) and (111) planes at 0.20 nm and 0.23 nm, respectively, which are close to previously reported data.[49] Since the RhNP were on top of TiO_2, the FFT results could not be assigned. Also, the catalysts were analysed by STEM-EDS and the elemental composition of the nanoparticles on the surface of TiO_2 was confirmed (Fig. 4). The heterojunction of Rh and TiO_2 was investigated by UV-vis DRS (Tauc plots in Fig. S3, ESI†). The influence of ionic liquids on TiO_2 was investigated by impregnation of [BMIm·OAc] on TiO_2. It was observed that the presence of the IL shifted down the bandgap value. The calculated direct band gaps of the impregnated Rh materials were shown to have increased values in comparison with pristine TiO_2 (Table 2). Upon increasing the metal content impregnated on TiO_2, the bandgap shifted to higher values. This behaviour is probably due to the overlap in the absorption spectra of the Rh colloids, ionic liquids, and TiO_2.

The electronic state of the Rh NPs synthesized was measured by XPS and the Rh 3d region is shown in Fig. 5 and in Table 2 (the survey spectrum can be found in the ESI,† Fig. S4). The data were acquired on the as-prepared non-supported nanoparticles, after isolation by centrifugation and washing with DI H_2O, due to the low Rh loading on the final catalyst. As the nanoparticles were of different sizes, the Rh 3d region shows an increase in the Rh^{x+} contribution in the smaller particles as already observed by others.[34,50,51] Two contributions from Rh^0 and Rh^{x+} were used for the deconvolution of the data with peaks at 307.0 and 309.2 eV, respectively.

The N_2 adsorption/desorption was evaluated for the catalysts synthesized in this work and showed similar behaviour for all catalysts, Fig. 6a, and the results are summarized in Table 3. The specific surface area, S_{BET}, was determined from the standard BET method and the total pore volume, V_p, was calculated at p/p_0 = 0.98–0.99 as shown in Table 3. The pore radius analysis, Fig. 6b, indicated a decreased porosity that is reflected in a lowered total pore volume and augmented average pore radius in RhNC and RhOh, as compared to RhNP.

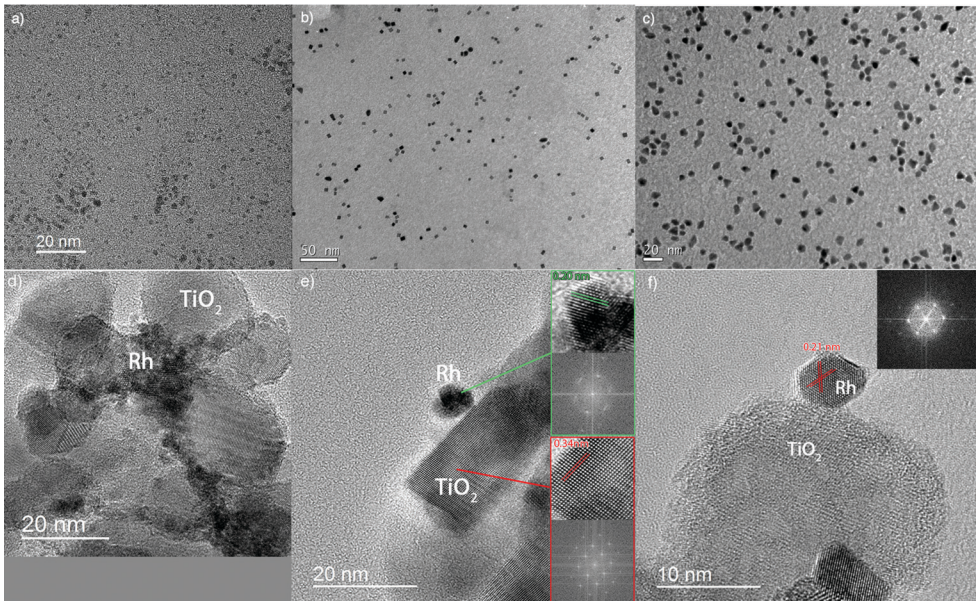

Fig. 3 TEM image of colloidal (a) RhNP, (b) RhNC, and (c) RhOh and HRTEM images of (d) RhNP, (e) RhNC showing the (200) atomic planes and corresponding FFT for Rh (green box) and TiO_2 (red box) and (f) a single RhOh nanoparticle on TiO_2 showing the (111) atomic planes of Rh and corresponding FFT (inset).

Table 2 Physico-chemical characterisation of the catalysts

System	TEM size (nm)	Rh amount FAAS (%)	Ratio Rh^0/Rh^{x+} [a] (%)	Bandgap [b] (eV)
TiO_2	—	—	—	3.20
RhNP	1.6 ± 0.4	0.24	38.8	3.58
RhNC	5.7 ± 0.7	0.09	63.2	3.40 [c]
RhOh	8.4 ± 1.7	0.11	78.1	3.47

[a] Determined by XPS analysis of unsupported nanoparticles. [b] Direct bandgap determined by linear extrapolation of Tauc plots. [c] Increasing the metal content to 0.56% (w/w) shifted the direct bandgap to 3.76 eV.

Hierarchically, the key alteration in the morphology occurs with aggregates and agglomerates of aggregates – one can see this by the elevated values of the fractal dimensions – from 2.44 (RhNP) up to 2.51 and 2.52 (RhNC and RhOh, respectively, shown in Fig. S5, ESI†). The rearrangement of the aggregated structure is especially visible comparing RhNC and RhOh, while at lower V_p (RhNC) the mesoporosity is maintained, as in the case of RhOh, *i.e.* the contributions of meso- and macropores are almost equal, whereas the size of TiO_2 primary particles did not undergo any alteration. Notice that RhNC and RhOh feature slightly enlarged rhodium nanoparticles giving an additional fraction despite their lower concentration in both hybrid catalysts in comparison to RhNP. Hence, a complex introduction of ionic liquids (1) and magnified Rh nanoparticles (2) leads to the decrease of empty volume (V_{em}) related to the true (ρ_0) and bulk (ρ_b) density of the powders: $V_{em} = 1/\rho_b - 1/\rho_0$, where the value of ρ_b undergoes an increase.

3.3. Photocatalytic H_2 production experiments

The H_2 production reactions were carried out at room temperature using a 10% methanol aqueous solution (10 mL) and 1.0 g L^{-1} catalyst concentration during a period of five hours (the kinetics of H_2 production of all catalysts is shown in Fig. 7). In the absence of MeOH the H_2 production was negligible; this is due to the fact that methanol is scavenging holes, decreasing recombination, but a part of H_2 is coming from photoreforming (coming from photooxidation) of methanol. A 25-fold increase in H_2 formation by the spherical nanoparticles in comparison with pristine TiO_2 and the colloidal nanoparticles was observed (up to 23.0 mmol g^{-1} of H_2 after 5 hours of reaction). Since RhNP were shown to have the smallest size among the Rh nanoparticles applied in this study, the number of particles on the surface of TiO_2 presents a higher number of active sites for the generation of H_2.

As shown in Fig. 8, the wavelength influence on the H_2 production can be also assessed upon the comparison of the H_2 production per gram of catalyst. The production per gram of catalyst of RhNP at 365 nm irradiation figures among the best results so far in these conditions (using commercial TiO_2 and methanol as a sacrificial reagent).[52] In comparison with other Rh catalysts under irradiation in the same region, our result is around 5 times better than previous reported, when normalized by the catalyst loading.[53] A comparison of other Rh-based catalysts can be found in Table S1 (ESI†), but direct comparison is difficult since different conditions were used, such as the choice of support, sacrificial reagent and irradiation wavelength/source.

Pristine TiO_2 showed the same production after five hours of reaction independent of the incident wavelength. However, by using the colloidal RhNP, it is clear that activation of the metallic surface upon irradiation at shorter wavelengths occurs. For non-plasmonic metals, interband transitions play a significant role in the light-activated catalysis.[54] Excitation of

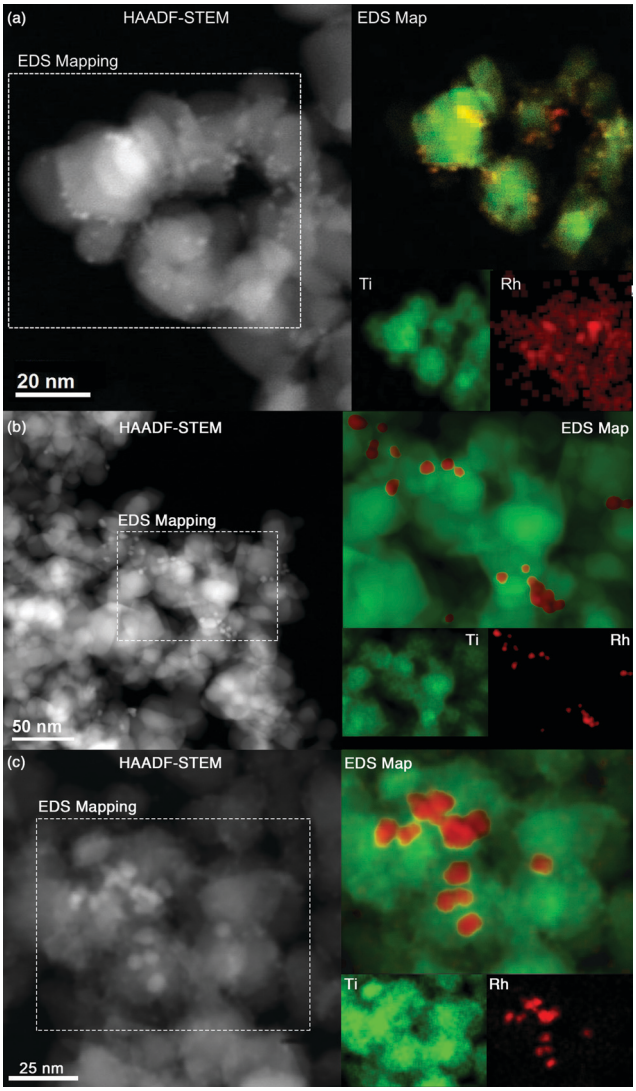

Fig. 4 HAADF-STEM/EDS of (a) RhNP, (b) RhNC and (c) RhOh, the inset presents the EDS mapping and individual contribution of Ti and Rh (colorized images).

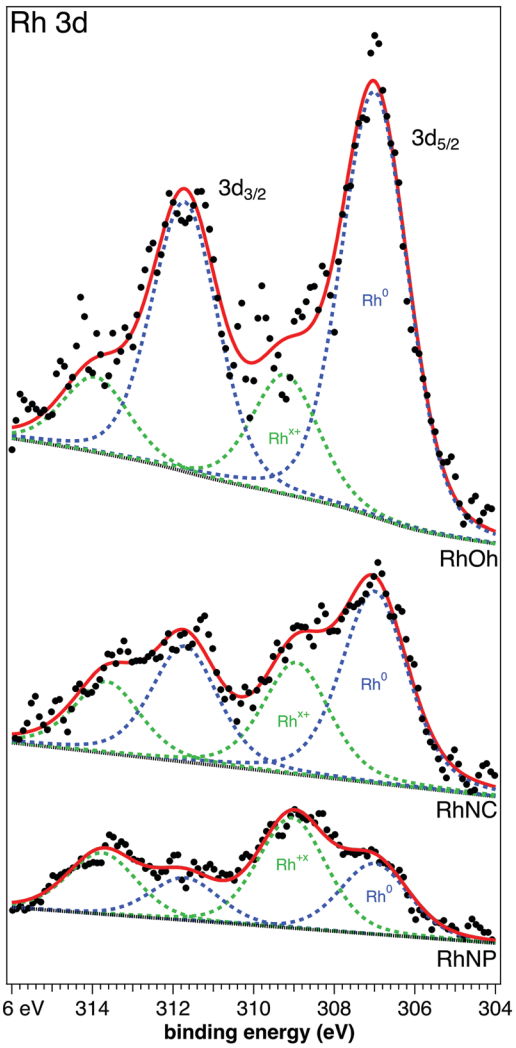

Fig. 5 XPS of the Rh 3d region of the nanoparticles synthesized in our work, highlighting the presence of both Rh^0 and Rh^{x+} contributions centred at 307.0 and 309.2 eV, respectively.

d-band electrons can be absorbed by the support and contribute to the generation of hot electrons and holes.[55] The excitation of d-band electrons can also interact with the LUMO of the adsorbed species at the surface of the Rh nanoparticles, therefore promoting the reaction (Table 4).

Although Rh nanocubes can exhibit localized surface plasmon resonance bands (LSPR),[56] the position of the plasmonic band depends on the size,[57] whereas the size of the RhNC is much smaller than the Rh nanocubes, which exhibit LSPR at the emission wavelengths of the LED used in this work. The position of the interband transitions of the Rh nanoparticles studied here overlaps with the absorption of UV light by TiO_2. Therefore, a dual-excitation pathway can lead to better efficiency in the generation of electron–hole pairs on TiO_2,[58] culminating in a strong synergetic effect in the catalysts. Upon preparing a catalyst with a higher amount of RhNC, the activity did not increase linearly (see Fig. S6, ESI†). This fact can be explained by an RhNC blocking out effect over TiO_2 light absorption that leads to lower activities.[59] Irradiation with a 300 W Xe lamp without a UV bandpass filter, commonly employed in solar simulation photocatalysis, didn't affect the catalyst performance as tested using RhNP (the comparison of the kinetics over 4 hours of reaction is shown in Fig. S7, ESI†). Therefore, we estimated that using visible light (>400 nm) would not increase the H_2 production, as observed by comparison of 365 nm and 400 nm LED lamps.

The specific rate of H_2 production was calculated after measuring the average size of the nanoparticles by TEM analysis, the rate of H_2 production and the amount of Rh on TiO_2 determined by FAAS, assuming that the surface in contact with TiO_2 was proportional for all samples[60] (see Table 4 and the ESI† for details). This mathematical approximation is similar to the previously estimated active surface areas of colloidal metal nanoparticles in heterogeneous reactions.[61] The specific rate of H_2 production was 3.0 μmol h^{-1} m^{-2} for pristine

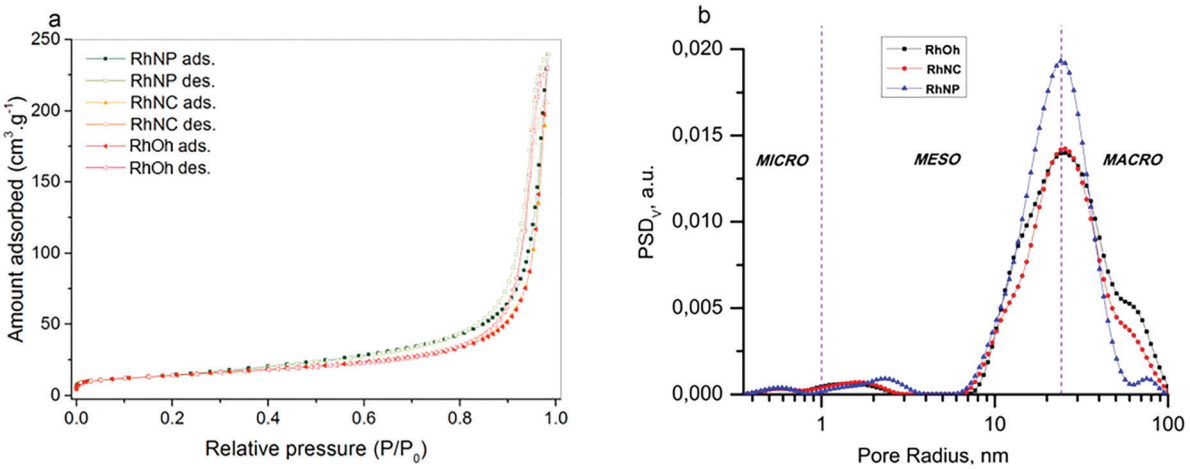

Fig. 6 (a) N_2 adsorption/desorption isotherms and (b) the pore size distribution by volume of the catalysts synthesized in this work.

Table 3 Textural characteristics of RhOh, RhNC and RhNP materials

Sample	S_{BET} ($m^2\ g^{-1}$)	V_p ($cm^3\ g^{-1}$)	V_{micro}/V_p (%)	V_{meso}/V_p (%)	V_{macro}/V_p (%)	R_p (nm)	D_S
RhOh	50	0.355	1.3	52.1	46.6	53	2.52
RhNC	50	0.317	1.5	54.3	44.3	49	2.51
RhNP	54	0.371	1.0	64.0	35.0	34	2.44

TiO_2 and 0.95 μmol h^{-1} m^{-2} for colloidal Rh at 365 nm, and 3.2 μmol h^{-1} m^{-2} and 0.19 μmol h^{-1} m^{-2} at 400 nm, respectively. Under these conditions, there is no dependency upon the incident wavelength of the UV-LED lamp using only TiO_2 as a catalyst. However, when Rh is impregnated on TiO_2 the H_2 production is highly dependent on the incident wavelength. For RhNP, the activity at 365 nm had a two-fold enhancement in comparison with the 400 nm irradiation. For the RhNC activity it was about a three-fold increase, while RhOh were shown to be not very dependent upon the incident wavelength, which constitutes evidence of better activity in the presence of [100] faceted NPs. Spherical (cuboctahedra) nanoparticles have both [111] and [100] facets on the surface,[37] and therefore showed an increase in activity for H_2 production. For RhNC, which are composed mainly of [100] exposed facets,[37] the activity was even higher at shorter wavelengths. Finally, for RhOh, whose surface is mainly composed of [111] facets, the activity remained almost unaltered. The higher activity of the RhNP, among the catalysts tested, could be associated with two main factors: (1) the higher concentration of Rh impregnated on TiO_2, and (2) the higher surface-to-volume ratio in comparison with the other Rh nanoparticles synthesised in this study. The stability of the catalysts before the reaction was assessed by conventional TEM, using both TiO_2-supported and unsupported RhNP (spheres) as shown in Fig. S8 (ESI†). Although it is difficult to perform good statistical counting on supported nanoparticles, is possible to observe that the size remains unaltered after the catalytic cycle, which is also true when using unsupported nanoparticles.

Upon normalising the average activity by surface area for the amount of Rh in each sample, it is possible to observe a higher activity of RhNC. The observed activity trend of RhNC > RhNP > RhOh is similar to earlier reports on Pd nanocubes and octahedra with different sizes for H_2 production in aqueous methanol.[62]

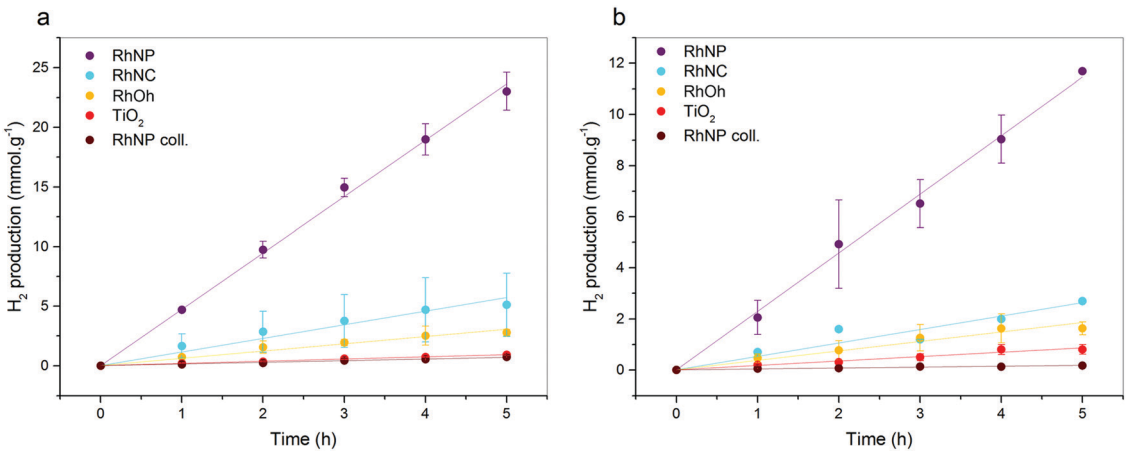

Fig. 7 Kinetic profiles of H_2 production over grams of catalyst per time, (a) at 365 nm irradiation and (b) at 400 nm irradiation.

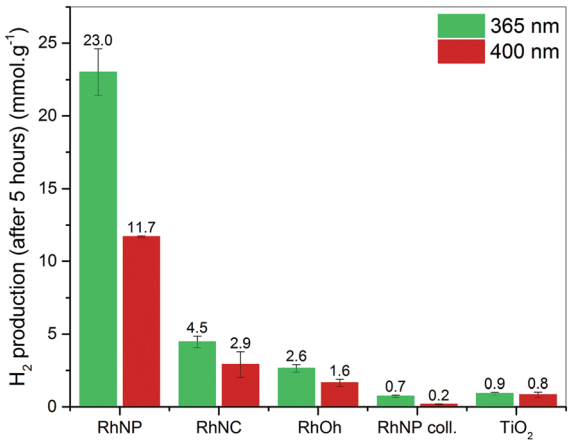

Fig. 8 Normalised H_2 production per gram of catalyst after 5 hours of reaction.

Table 4 Specific rate of H_2 production and relative photonic efficiency, ζ_r, of the catalysts upon different incident wavelengths

	Specific rate[a] (mmol h^{-1} m^{-2})		ζ_r (%)	
System	365 nm	400 nm	365 nm	400 nm
TiO_2	3.0×10^{-3} [b]	3.2×10^{-3} [b]	2.7	2.7
RhNP	13.5	5.6	73.8	30.6
RhNC	22.4	7.5	26.1	8.7
RhOh	7.9	5.2	9.2	6.2
RhNP[c]	9.5×10^{-4}	1.9×10^{-4}	0.08	0.02

[a] Values were determined by the linear fit of the slope of the H_2 production kinetics in a 5 hour reaction at room temperature, the reported data are an average of at least three independent experiments. [b] Specific rate calculated using the BET surface area value (56 m^2 g^{-1}). [c] Colloidal nanoparticles.

The higher activity of the RhNC might be due to the higher surface energy of the Rh nanoparticles, in comparison with other metals such as Au, Pt, and Pd, regardless of their shape.[63] The higher activity observed for the RhNC and RhNP could be an effect of the presence of imidazolium ionic liquids in their preparation. It is well known that the interaction of imidazolium cations with the metal nanoparticle surface could produce metal-N-heterocyclic carbene species (M-NHC)[64–66] and consequently different catalytic activities. To confirm the influence of the IL in water photolysis, the RhOh catalyst was treated with [BMIm·OAc] and TGA analysis showed that 2 wt% remained on TiO_2 (Fig. S9, ESI†). The small increase in activity after impregnation with the IL (Fig. S10, ESI†) can be explained by two different mechanisms: (1) the formation of Rh–NHC carbene species at the surface[65] and (2) the interaction of the ionic pair with the TiO_2 surface, which synergically shifts the bandgap.[67] The bandgap for the IL-doped RhOh also decreased from 3.47 to 3.44 eV, a difference of 0.03 eV, which is similar to the 0.05 eV difference when doping TiO_2 with the IL. This result is evidence of IL cation participation in the photocatalytic effect as observed before.[67]

ζ_r was determined and since the estimation was carried out using the same catalyst loading and LED lamps in our study, an apparent quantum efficiency (Φ_{app}) was not used in this study. The results are compiled in Table 4. It can be noted that all Rh-impregnated catalysts showed better efficiency than pristine TiO_2. The high ζ_r values obtained in this work are also observable in the high H_2 production of all catalysts, especially the RhNP, which converted approximately ~74% of photons to H_2. Similar ζ_r values for equivalent H_2 production have been observed before,[68] but referred to as the apparent quantum efficiency, Φ_{app}. The discussion of using Φ_{app} for heterogeneous photocatalysis can be found elsewhere.[46,69] Also, the reactor design may play a major role since the sample is irradiated in all directions, minimizing the scattering effects of the powdered sample. The higher efficiency of the systems at lower wavelength is probably due to the better photon absorption by TiO_2 and therefore better charge transfer to the co-catalyst. TiO_2 exhibited the same ζ_r for both wavelengths, due to its absorption spectra in the UV region. In the case of RhOh, the ζ_r difference between the wavelengths is less evident, 9.2% *versus* 6.2% for 365 nm and 400 nm, respectively. This effect for Rh photocatalysis was also observed in the photodegradation of 4-chlorophenol by UV and visible light.[70]

4. Conclusions

The results presented in this paper show that the photocatalytic activity is directly related to the exposed facets of the Rh-cocatalyst and they can be tailored by the shape of MNPs. The H_2 production is among the best reported so far using UV LED lamps and commercial TiO_2. Despite using Rh as a cocatalyst, it was observed that a very low amount of impregnation (*i.e.* RhNP at 0.24%) is enough to achieve a hydrogen production of about 4.68 mmol h^{-1} per gram of catalyst. A triple synergic effect of TiO_2, Rh nanoparticles and the ionic liquid was observed. The incident photon energy was also an important observation in this work. With only a few nanometre difference in the UV-LED emission, there was an increase of about 30% in the H_2 production activity and ζ_r using spherical and cubic nanoparticles. The application of the magic number approach to unveil the surface activity of the catalysts was essential to rationalize the morphological effects. All of these observations reveal a trend in the H_2 production of the exposed facets [100] > [111] in the studied conditions. The hydrogen generation presented in this work figures among the best reported so far for rhodium co-catalysts impregnated on TiO_2. Also, common LED strips can be used as a photon source for the production of hydrogen in aqueous methanolic solutions. This can be applied to different alcohols to seek more environmentally friendly H_2 production. The electric energy demand for LED light sources shows good potential for sunlight powered systems with the aid of common photovoltaic cells.

Conflicts of interest

There are no conflicts to declare.

Acknowledgements

The authors are thankful for financial support from CAPES (158804/2017-01 and 001), FAPERGS (16/2552-0000 and 18/2551-0000561-4), and CNPq (406260/2018-4, 406750/2016-5 and 465454/2014-3). We are grateful to the National Laboratory of Nanotechnology (LNNano-Campinas) under proposal TEM-24375 for the HRTEM analysis, the Central Laboratory of Electron Microscopy (LCME) at UFSC for the TEM analysis, the Laboratory of Atomic Spectrometry at IQ-UFRGS for the FAAS analysis and Prof. Claudio Radtke (UFRGS) for XPS experiments.

Notes and references

1 A. Fujishima and K. Honda, *Nature*, 1972, **238**, 37–38.
2 K. Hashimoto, H. Irie and A. Fujishima, *Jpn. J. Appl. Phys.*, 2005, **44**, 8269–8285.
3 G. R. Bamwenda, S. Tsubota, T. Nakamura and M. Haruta, *J. Photochem. Photobiol., A*, 1995, **89**, 177–189.
4 M. Ni, M. K. H. Leung, D. Y. C. Leung and K. Sumathy, *Renewable Sustainable Energy Rev.*, 2007, **11**, 401–425.
5 J. Yu, L. Qi and M. Jaroniec, *J. Phys. Chem. C*, 2010, **114**, 13118–13125.
6 L. Liu, H. Zhao, J. M. Andino and Y. Li, *ACS Catal.*, 2012, **2**, 1817–1828.
7 M. I. Qadir, M. Zanatta, E. S. Gil, H. K. Stassen, P. Gonçalves, B. A. D. Neto, P. E. N. de Souza and J. Dupont, *ChemSusChem*, 2019, **12**, 1011–1016.
8 J. Yu, J. Low, W. Xiao, P. Zhou and M. Jaroniec, *J. Am. Chem. Soc.*, 2014, **136**, 8839–8842.
9 H. Dong, G. Zeng, L. Tang, C. Fan, C. Zhang, X. He and Y. He, *Water Res.*, 2015, **79**, 128–146.
10 B. Sirota, J. Reyes-Cuellar, P. Kohli, L. Wang, M. E. McCarroll and S. M. Aouadi, *Thin Solid Films*, 2012, **520**, 6118–6123.
11 S. Sood, A. Umar, S. Kumar Mehta and S. Kumar Kansal, *Ceram. Int.*, 2015, **41**, 3355–3364.
12 D. M. Schultz and T. P. Yoon, *Science*, 2014, **343**, 1239176.
13 M. Oelgemoller, *Chem. Rev.*, 2016, **116**, 9664–9682.
14 W. K. Jo and R. J. Tayade, *Ind. Eng. Chem. Res.*, 2014, **53**, 2073–2084.
15 M. P. Languer, F. R. Scheffer, A. F. Feil, D. L. Baptista, P. Migowski, G. J. Machado, D. P. de Moraes, J. Dupont, S. R. Teixeira and D. E. Weibel, *Int. J. Hydrogen Energy*, 2013, **38**, 14440–14450.
16 R. V. Gonçalves, H. Wender, P. Migowski, A. F. Feil, D. Eberhardt, J. Boita, S. Khan, G. Machado, J. Dupont and S. R. Teixeira, *J. Phys. Chem. C*, 2017, **121**, 5855–5863.
17 T. N. Ravishankar, M. de, O. Vaz, T. Ramakrishnappa, S. R. Teixeira, J. Dupont, R. K. Pai and G. Banuprakash, *J. Mater. Sci.*, 2018, **29**, 11132–11143.
18 S. Cao, J. Jiang, B. Zhu and J. Yu, *Phys. Chem. Chem. Phys.*, 2016, **18**, 19457–19463.
19 S. Fodor, G. Kovács, K. Hernádi, V. Danciu, L. Baia and Z. Pap, *Catal. Today*, 2017, **284**, 137–145.
20 H. Kotani, R. Hanazaki, K. Ohkubo, Y. Yamada and S. Fukuzumi, *Chem. – Eur. J.*, 2011, **17**, 2777–2785.
21 Y.-F. Li and Z.-P. Liu, *J. Am. Chem. Soc.*, 2011, **133**, 15743–15752.
22 M. Luo, P. Lu, W. Yao, C. Huang, Q. Xu, Q. Wu, Y. Kuwahara and H. Yamashita, *ACS Appl. Mater. Interfaces*, 2016, **8**, 20667–20674.
23 M. Luo, W. Yao, C. Huang, Q. Wu and Q. Xu, *RSC Adv.*, 2015, **5**, 40892–40898.
24 T. S. Rodrigues, A. G. M. da Silva and P. H. C. Camargo, *J. Mater. Chem. A*, 2019, **7**, 5857–5874.
25 Y. Xia, X. Xia and H.-C. Peng, *J. Am. Chem. Soc.*, 2015, **137**, 7947–7966.
26 Y. Xia, Y. Xiong, B. Lim and S. E. Skrabalak, *Angew. Chem., Int. Ed.*, 2009, **48**, 60–103.
27 S. Xie, X. Y. Liu and Y. Xia, *Nano Res.*, 2015, **8**, 82–96.
28 Z. Huang, J. Gong and Z. Nie, *Acc. Chem. Res.*, 2019, **52**, 1125–1133.
29 H. Tada, *Dalton Trans.*, 2019, **48**, 6308–6313.
30 S. Cao, H. Li, Y. Li, B. Zhu and J. Yu, *ACS Sustainable Chem. Eng.*, 2018, **6**, 6478–6487.
31 M. Luo, W. Yao, C. Huang, Q. Wu and Q. Xu, *J. Mater. Chem. A*, 2015, **3**, 13884–13891.
32 M. Luo, P. Lu, W. Yao, C. Huang, Q. Xu, Q. Wu, Y. Kuwahara and H. Yamashita, *ACS Appl. Mater. Interfaces*, 2016, **8**, 20667–20674.
33 F. Xue, C. Chen, W. Fu, M. Liu, C. Liu, P. Guo and S. Shen, *J. Phys. Chem. C*, 2018, **122**, 25165–25173.
34 Y. Zhang, D. A. J. M. Ligthart, X.-Y. Quek, L. Gao and E. J. M. Hensen, *Int. J. Hydrogen Energy*, 2014, **39**, 11537–11546.
35 T. Ikeda, A. Xiong, T. Yoshinaga, K. Maeda, K. Domen and T. Teranishi, *J. Phys. Chem. C*, 2012, **117**, 2467–2473.
36 A. P. Umpierre, E. de Jesus and J. Dupont, *ChemCatChem*, 2011, **3**, 1413–1418.
37 Y.-J. Wang, W. Long, L. Wang, R. Yuan, A. Ignaszak, B. Fang and D. P. Wilkinson, *Energy Environ. Sci.*, 2018, **11**, 258–275.
38 T. N. Nguyen, S. Kampouri, B. Valizadeh, W. Luo, D. Ongari, O. M. Planes, A. Züttel, B. Smit and K. C. Stylianou, *ACS Appl. Mater. Interfaces*, 2018, **10**, 30035–30039.
39 J. N. Demas, W. D. Bowman, E. F. Zalewski and R. A. Velapoldi, *J. Phys. Chem.*, 1981, **85**, 2766–2771.
40 C. Hubert, E. G. Bilé, A. Denicourt-Nowicki and A. Roucoux, *Green Chem.*, 2011, **13**, 1766–1771.
41 P. A. Webb, C. Orr, R. W. Camp, J. P. Olivier and Y. S. Yunes, *Analytical Methods in Fine Particle Technology*, Micrometrics Instrument, 1st edn, 1997.
42 V. M. Gun'ko and D. D. Do, *Colloids Surf., A*, 2001, **193**, 71–83.
43 V. M. Gun'ko, *Appl. Surf. Sci.*, 2014, **307**, 444–454.
44 C. Nguyen and D. D. Do, *Langmuir*, 1999, **15**, 3608–3615.
45 C. Nguyen and D. D. Do, *Langmuir*, 2000, **16**, 7218–7222.
46 N. Serpone, *J. Photochem. Photobiol., A*, 1997, **104**, 1–12.
47 W.-K. Jo and R. J. Tayade, *Ind. Eng. Chem. Res.*, 2014, **53**, 2073–2084.
48 G. Matafonova and V. Batoev, *Water Res.*, 2018, **132**, 177–189.

49 A. J. Biacchi and R. E. Schaak, *ACS Nano*, 2015, **9**, 1707–1720.
50 V. Cimpeanu, M. Kočevar, V. I. Parvulescu and W. Leitner, *Angew. Chem., Int. Ed.*, 2009, **48**, 1085–1088.
51 M. E. Grass, Y. Zhang, D. R. Butcher, J. Y. Park, Y. Li, H. Bluhm, K. M. Bratlie, T. Zhang and G. A. Somorjai, *Angew. Chem., Int. Ed.*, 2008, **47**, 8893–8896.
52 R. Singh and S. Dutta, *Fuel*, 2018, **220**, 607–620.
53 T. H. Chiang, H. Lyu, T. Hisatomi, Y. Goto, T. Takata, M. Katayama, T. Minegishi and K. Domen, *ACS Catal.*, 2018, **8**, 2782–2788.
54 S. Sarina, H.-Y. Zhu, Q. Xiao, E. Jaatinen, J. Jia, Y. Huang, Z. Zheng and H. Wu, *Angew. Chem., Int. Ed.*, 2014, **53**, 2935–2940.
55 X. Zhang, Y. L. Chen, R.-S. Liu and D. P. Tsai, *Rep. Prog. Phys.*, 2013, **76**, 046401.
56 A. M. Watson, X. Zhang, R. Alcaraz de la Osa, J. M. Sanz, F. González, F. Moreno, G. Finkelstein, J. Liu and H. O. Everitt, *Nano Lett.*, 2015, **15**, 1095–1100.
57 X. Zhang, P. Li, Á. Barreda, Y. Gutiérrez, F. González, F. Moreno, H. O. Everitt and J. Liu, *Nanoscale Horiz.*, 2016, **1**, 75–80.
58 X. Zhang, Y. L. Chen, R.-S. Liu and D. P. Tsai, *Rep. Prog. Phys.*, 2013, **76**, 046401.
59 T. Hisatomi, K. Maeda, K. Takanabe, J. Kubota and K. Domen, *J. Phys. Chem. C*, 2009, **113**, 21458–21466.
60 D. Faggion Junior, R. Haddad, F. Giroud, M. Holzinger, C. E. Maduro de Campos, J. J. S. Acuña, J. B. Domingos and S. Cosnier, *Nanoscale*, 2016, **8**, 10433–10440.
61 A. M. Signori, K. d. O. Santos, R. Eising, B. L. Albuquerque, F. C. Giacomelli and J. B. Domingos, *Langmuir*, 2010, **26**, 17772–17779.
62 F. Xue, C. Chen, W. Fu, M. Liu, C. Liu, P. Guo and S. Shen, *J. Phys. Chem. C*, 2018, **122**, 25165–25173.
63 S. Xie, X. Y. Liu and Y. Xia, *Nano Res.*, 2015, **8**, 82–96.
64 F. Bernardi, J. D. Scholten, G. H. Fecher, J. Dupont and J. Morais, *Chem. Phys. Lett.*, 2009, **479**, 113–116.
65 L. S. Ott, M. L. Cline, M. Deetlefs, K. R. Seddon and R. G. Finke, *J. Am. Chem. Soc.*, 2005, **127**, 5758–5759.
66 G. Chacón, J. Durand, I. Favier, E. Teuma and M. Gomez, *Fr. Ukr. J. Chem.*, 2016, **4**, 23–36.
67 H. Weber and B. Kirchner, *ChemSusChem*, 2016, **9**, 2505–2514.
68 W. Wang, S. Liu, L. Nie, B. Cheng and J. Yu, *Phys. Chem. Chem. Phys.*, 2013, **15**, 12033–12039.
69 A. Salinaro, A. V. Emeline, J. Zhao, H. Hidaka, V. K. Ryabchuk and N. Serpone, *Pure Appl. Chem.*, 1999, **71**, 321–335.
70 L. Zang, W. Macyk, C. Lange, W. F. Maier, C. Antonius, D. Meissner and H. Kisch, *Chem. – Eur. J.*, 2000, **6**, 379–384.

